Title

Reconstruction of 4-D Dynamic SPECT Images from Inconsistent Projections Using a Spline Initialized FADS Algorithm (SIFADS)

Journal

IEEE Transactions on Medical Imaging, 34(1)

ISSN

0278-0062

Authors

Abdalah, Mahmoud
Boutchko, Rostyslav
Mitra, Debasis
et al.

Publication Date

2015

DOI

10.1109/tmi.2014.2352033

Peer reviewed

Reconstruction of 4D Dynamic SPECT Images from Inconsistent Projections Using a Spline Initialized FADS Algorithm (SIFADS)

Mahmoud Abdalah*, Rostyslav Boutchko†, *Member, IEEE,* Debasis Mitra*, *Senior Member, IEEE,* and Grant T. Gullberg†, *Fellow, IEEE*

***Abstract*—In this work we propose and validate an algorithm of extracting voxel-by-voxel time activity curves directly from inconsistent projections applied in dynamic cardiac SPECT. The algorithm was derived based on factor analysis of dynamic structures (FADS) approach and imposes prior information by applying several regularization functions with adaptively changing relative weighting. The anatomical information of the imaged subject was used to apply the proposed regularization functions adaptively in the spatial domain. The algorithm performance is validated by reconstructing dynamic datasets simulated using the NCAT phantom with a range of different input tissue time-activity curves. The results are compared to the spline-based and FADS methods. The validated algorithm is then applied to reconstruct pre-clinical cardiac SPECT data from canine and murine subjects. Images, generated from both simulated and experimentally acquired data confirm the ability of the new algorithm to solve the inverse problem of dynamic SPECT with slow gantry rotation.**

***Index Terms*—Dynamic SPECT, Image Reconstruction, Regularization, Optimization.**

I. Introduction

DYNAMIC single photon emission computed tomography (SPECT) aims to estimate the concentration distribution of a gamma-ray emitting tracer inside a patient body as its concentration changes with time. The temporal variation of the concentration provides important information about radiotracer pharmacokinetics and about the physiology of tissues and organs [1]. The main challenge of dynamic SPECT is insufficient temporal resolution [1], [2]. For example, in dynamic cardiac SPECT imaging, the characteristic time of a significant change in the imaged distribution during the input of the tracer is on the order of seconds, while a typical modern dual-head scanner requires more than half a minute to acquire a minimal geometrically consistent dataset [3]. This temporal resolution mismatch prevents one from applying the intuitive approach, where the dynamic problem is solved as a series of static reconstructed images independently generated from repeated scans.

The technical goal of dynamic imaging is to determine the time-varying intensity in each image voxel, also known as the time activity curve (TAC). Hardware limitations of the camera and high noise contamination of the signal caused by dose considerations make TAC determination in SPECT a highly under-determined problem that can only be solved as an optimization problem with constraints to reduce the dimensionality of the problem.

Our underlying hypothesis is that the spatiotemporal tracer distribution can be obtained as a single four-dimensional (4D) solution to an optimization problem of fitting dynamic SPECT projections with a number of imposed constraints. The dynamic SPECT problem is solved in 4D by constraining the temporal dimensions of the unknown voxel values to a small number of functional forms with additional spatial and temporal regularization terms based on prior knowledge.

Direct 4D reconstruction by constraining the temporal component of the unknown distribution to a few functional forms common for the entire reconstruction domain was first implemented using a spline-based approach [5]. In this approach, individual voxel TACs are expanded in terms of several preset functions, and the expansion coefficients for each voxel are determined by the reconstruction process. The TACs are represented as a linear combination of a limited number of preset time basis functions. The use of exponential-based time functions was proposed in [4], and B-spline basis functions were proposed in [5], [6]. An application of the B-spline approach to dynamic pinhole SPECT is given in [7] and most recently in [8]. Using preset temporal functions has been shown to produce meaningful results; however, the TACs obtained with this method are sometimes over-smoothed, imprecise for some types of input functions, and not always reliable for quantitation purposes.

An alternative approach to direct 4D reconstruction is based on factor analysis of dynamic structures (FADS) [9], which is a technique used in the analysis of dynamic sequences. FADS can be used for automatic extraction of TACs for different tissue types from reconstructed dynamic images, as well as extraction of TACs directly from dynamic projections with no prior reconstruction. In FADS, the shape of time-dependent basis functions or *factors* is determined by the reconstruction algorithm along with the expansion coefficients for each voxel. As a result, it is argued that FADS determines the optimal time basis functions for a dynamic tracer distribution. The FADS technique has been previously applied in dynamic SPECT in [10]-[13]. In these applications, however, the reconstruction algorithm was highly sensitive to the initial choice of the number

Manuscript received December 18, 2013; revised August 15, 2014. Corresponding author: M. Abdalah (Computer Science Department, Florida Institute of Technology, 150 West University Blvd. Melbourne, Florida, 32901. Phone: 614-316-6039, Email: mabdalah2009@my.fit.edu)

*M. Abdalah and D. Mitra are with Florida Institute of Technology.

†R. Boutchko and G. T. Gullberg are with Lawrence Berkeley National Laboratory.

and type of factors, becoming unstable with an inappropriate choice of the shape. As a result, the signal to noise ratio (SNR) and accuracy were significantly reduced. These reports suggest that direct application of this method may be overly sensitive to the initial selection of the number of factors or otherwise unstable.

Other methods have been proposed for the dynamic SPECT problem such as dSPECT, which tries to estimate the time activity curves for each voxel without factoring the activity into temporal components. However, this method may result in reconstructions with poor contrast between tissue types due to insufficient constraints [14]-[16].

In this work, we propose a 4D reconstruction algorithm SIFADS or *spline-initialized factor analysis of dynamic structures* that estimates time activity curves from the inconsistent data generated in dynamic SPECT. The algorithm estimates TACs from data acquired during the first rotation after the tracer injection when its concentration is changing quickly with respect to the speed of the camera rotation. The algorithm is an extension of FADS with several adaptively weighted regularization terms that impose anatomical constraints and temporal smoothness.

We compared three algorithms in this work: a spline-based method, FADS, and SIFADS. The theory of our approach and the algorithms used to implement it are described in Section II. In Section III, we describe the numerical simulations used to validate our method and the dynamic SPECT experiments to which our algorithm was applied. In Section IV, we present validation results from numerical simulations and from real dynamic scans. Finally, our conclusions are presented in Section VI.

II. Methods: Theory and Algorithms

A. Dynamic SPECT

The forward problem in static SPECT (when tracer concentration is assumed to be invariant in time) is defined as

$$P_n = \sum_k S_{n,k} V_k, \tag{1}$$

where V_k is the intensity of the k^{th} voxel where $k = 1, \ldots, K$; $S_{n,k}$ is the matrix element of the *system matrix* that describes the geometrical parameters and physical properties of the imaging system; and P_n is the expected counts detected in the n^{th} projection, $n = 1, \ldots, N$. The inverse problem or image reconstruction, when the values V_k are computed from projections P_n, is usually solved by applying iterative inversion algorithms that take into account the statistical properties of the noisy projection data.

In dynamic SPECT, the imaged volume changes with time while the projections are being acquired. We assume the acquisition time is discretized into I short time intervals defined by their endpoints t_i. Assuming $t_0 \equiv 0$, the dynamic projection is defined as

$$P_n(t_i) = \int_{t_{i-1}}^{t_i} \sum_k S_{n,k} V_k(t)\, dt. \tag{2}$$

In all the examples in this manuscript, we use uniform temporal intervals $\Delta t_i = t_i - t_{i-1}$ equal to one second, the minimum allowable single projection acquisition time for our SPECT scanner. Non-uniform Δt_i could also be used.

Unlike in PET or some multi-pinhole SPECT scanners, a SPECT scanner with rotating gantry cannot acquire a complete dataset sufficient for the reconstruction of the $V(t_i)$ during a single time frame. In fact, for each t_i only one or two projection views can be acquired by a typical SPECT system. Denoting the number of projection bins in a single detector head by N_{view}, we can formalize the relation between the temporal interval index i and the general projection bin index n in (2) for a two-head scanner. Assuming that the projection index n is always formed by first running through the projection bins of the two detector heads for a fixed projection angle and then incrementing the index by $2N_{\text{view}}$, we have

$$i = \lceil n/(2N_{\text{view}}) \rceil, \tag{3}$$

where $\lceil x \rceil$ denotes the ceiling of x: the smallest integer larger than or equal to x. Then,

$$P_n \equiv P_n(t_i)|_{i=\lceil n/(2N_{\text{view}}) \rceil} = \int_{t_{i-1}}^{t_i} \sum_k S_{n,k} V_k(t)\, dt. \tag{4}$$

In order to reduce the dimensionality of the problem, we expand the time-dependent voxel intensities $V_k(t)$ as a linear combination of a small number J of time-dependent basis functions or *factors* $f_j(t)$; $j = 1, \ldots, J$. These functions typically describe the temporal behavior of the tracer concentrations in different tissue types. When using a discrete representation for both the volume and the factor arrays, the intensity of the k^{th} voxel is

$$V_{k,i} = \frac{1}{\Delta t_i} \int_{t_{i-1}}^{t_i} V_k(t)\, dt = \sum_j C_{k,j} f_{j,i}, \tag{5}$$

where

$$f_{j,i} = \int_{t_{i-1}}^{t_i} f_j(t)\, dt.$$

The desired, discrete 4D tracer distribution $V_{k,i}$ is fully described by the time basis vectors f and the coefficient array C. Combining the above model of the tracer dynamics (5) with the forward propagation expression (4), we obtain the desired model of the dynamic sinogram projection data:

$$P_n = \sum_k \left(S_{n,k} \sum_j C_{k,j} f_{j,i} \right) \Bigg|_{i=\lceil n/(2N_{\text{view}}) \rceil}, \tag{6}$$

or, in matrix notation:

$$P = SCf. \tag{7}$$

When the system matrix S is known and the acquired projections array P follows a Poisson distribution, we propose to solve the dynamic tomographic problem (variable sets f and C) by maximizing the following log likelihood function;

$$\mathcal{L}(P|C,f) = \sum_{i,n} \Bigg(- \sum_{k,j} S_{n,k} C_{k,j} f_{j,i} + P_n \log \Big(\sum_{k,j} S_{n,k} C_{k,j} f_{j,i} \Big) - \log(P_n!) \Bigg) \Bigg|_{i=\lceil n/(2N_{\text{view}}) \rceil}. \tag{8}$$

In order to estimate the desired solution of (8), we propose to choose J, the number of factors, close to the number of tissue types to be separated. In order to handle the limitations of insufficient angular sampling for each time frame i, we impose a number of regularization functions and then develop an algorithm based on the FADS approach.

Our primary objective is to find the voxel TACs defined in (5). The values of f and C are not important as long as the result of their multiplication matches the true TACs as close as possible.

B. Regularization Constraints

In this work, a number of constraints are used to solve the dynamic tomography optimization problem. In order to determine the necessary constraints, we employ the following considerations: (i) *Tissue separation* is expected throughout most of the region of reconstruction. Therefore, we expect voxels that do not contain organ boundaries to be occupied by a single tissue type, such as myocardium, liver, blood, or a type of tissue that does not exhibit significant tracer uptake. This means that for any voxel k, only one of the J coefficients $C_{k,j}$ can be significantly larger than zero. At this stage, we do not take into account potential inhomogeneities of the functional form of the TAC within any specific organ. We do expect the factor functions to closely represent the TACs within the largest single-tissue segments, such as the blood cavity, the heart muscle, or the liver. (ii) *Piecewise spatial smoothness* means that the change of tracer concentration within a single tissue type has to be smooth. Therefore, for a fixed j, coefficients $C_{k,j}$ within the region of the same tissue type must not have large variations. (iii) *Temporal smoothness* arises from the nature of the tracer kinetics, although smoothness of $f_{j,t}$ is constrained separately for each tissue type j. (iv) Non-negativity of the tracer distribution is preserved by enforcing non-negativity of all $f_{j,t}$ and $C_{k,j}$ values.

Algorithmically, the proposed constraints are implemented by adding terms to the likelihood function (8) to be maximized [17], [18]:

$$\hat{\mathcal{L}}(P|C,f) = \mathcal{L}(P|C,f) - \lambda_1\Omega(C) - \lambda_2\Theta(C) - \lambda_3\Phi(f). \quad (9)$$

The detailed expressions for the tissue separation constraint Ω, piecewise spatial smoothness constraint Θ, and temporal smoothness constraint Φ are given at the end of this section. The relative weights of these terms are regulated by the scalar weighting parameters λ_1, λ_2, and λ_3. These parameters are adjusted adaptively during the reconstruction procedure as explained in Section II-D.

The first two of the proposed constraints rely on having a prior estimate of the location of the different tissues. This prior estimate is introduced in terms of a (non-binary) integer mask computed from two binary masks. This integer mask is further refined during the reconstruction process. The two binary masks are computed as follows:

- First, a $J \times K$ binary ***static mask*** $\mathbb{M}^s$ is computed. Tracer concentration changes rapidly during only the first gantry rotation. Changes over subsequent rotations are slow enough to perform a static reconstruction for each rotation. We aggregate data from all rotations except the first one to create a reconstructed image with lower noise for the purpose of generating masks for myocardium, blood pool (the left-ventricular cavity), and liver. Specifically, the reconstructed static image is first segmented into tissue regions, then the mask elements $\mathbb{M}^s_{kj}$ are equal to one in the identified tissue region and zero otherwise:

$$\mathbb{M}^s_{k,j} = \begin{cases} 1, & \text{voxel } k \text{ is within tissue type } j \\ 0, & \text{otherwise.} \end{cases} \quad (10)$$

- Second, at each iteration of the dynamic reconstruction algorithm described in the next subsection, a ***dynamic mask*** $\mathbb{M}^d$ is computed by simple thresholding of the current value of the elements in the coefficient array C:

$$\mathbb{M}^d_{k,j} = \begin{cases} 0, & \text{if } C_{k,j} \geq \tau_j, \\ 1, & \text{if } C_{k,j} < \tau_j, \end{cases} \quad (11)$$

where the user defined thresholds τ_j are selected to generate segments with areas similar or slightly exceeding those in the static mask $\mathbb{M}^s$.

- Finally, the integer mask is determined in terms of the intersection between $\mathbb{M}^s$ and $\mathbb{M}^d$ as follows:

$$\mathbb{M}_{k,j} = \begin{cases} 0, & \text{if } \mathbb{M}^s_{k,j} = \mathbb{M}^d_{k,j} = 0, \\ j, & \text{if } \mathbb{M}^s_{k,j} = \mathbb{M}^d_{k,j} = 1, \\ -1, & \text{otherwise.} \end{cases} \quad (12)$$

This masking relates voxels to the corresponding factor (j), or uncertain region (-1), or region of non-interest (0). The exact value of the unique integer identifier constant (-1) is irrelevant as long as it cannot be confused with other elements. The definition of this final mask is updated after each reconstruction iteration. In Fig. 1, the mask creation algorithm is illustrated graphically.

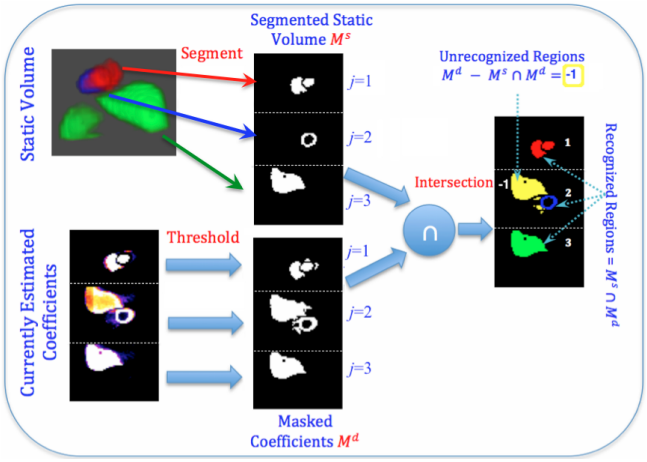

Fig. 1. Integer masks (1-3, -1) are created for each of the three tissue types and one for the uncertain region type using the intersection of (i) a static mask M^S creating by preprocessing the consistent data from later rotations, and (ii) a dynamic mask.

The three regularization terms are defined below:

- *Tissue separation* $\Omega(C, \mathbb{M})$ is a penalty function that discourages a voxel to have mixed tissue types. This term

is a scalar product of the coefficient vectors, defined similarly as the regularization term in [11], but applied only to the voxels in uncertain regions where the coefficient mixing is undesired:

$$\Omega(C,\mathbb{M}) = \sum_{k,j}^{K,J} \Big(\sum_{i|i\neq j}^{J} |C_{k,j}\cdot C_{k,i}| \cdot \delta(\mathbb{M}_{k,j}\ ,-1)\Big), \tag{13}$$

where δ is the delta function as defined by:

$$\delta(a,b) = \begin{cases} 1, & a=b, \\ 0, & \text{otherwise.} \end{cases} \tag{14}$$

For voxels within well-segmented tissue types, we presume the coefficient values to be close to one.

- *Spatial smoothness* $\Theta(C,\mathbb{M})$ is an *anisotropic total variation* (ATV) function [25] applied to the voxels that belong to the same tissue type. This technique allows the algorithm to smooth the regions within the same tissue type while the boundaries and edges are preserved:

$$\Theta(C,\mathbb{M}) = \sum_{k,j} \Big(\sum_{n\in\{N_k\}} |C_{k,j} - C_{n,j}| \cdot \delta(\mathbb{M}_{k,j},\mathbb{M}_{n,j})\Big), \tag{15}$$

where $\{N_k\}$ is the set of the k^{th} voxel's immediate neighbors.

- *Temporal Smoothing* function $\Phi(f)$ minimizes the differences between the time factor arrays:

$$\Phi(f) = \sum_{j=1}^{J}\sum_{t=2}^{T} |f_{j,t} - f_{j,t-1}|. \tag{16}$$

C. Optimization Procedure

Our algorithm is a combination of the spline-based and the FADS algorithms, thus we refer to it as the *spline initialized factor analysis of dynamic structures* (SIFADS). The SIFADS procedure consists of three stages:

1) *Data preparation*: forming the dynamic projection dataset (timeframes from the first rotation) and the static datasets (sum of the data from all subsequent rotations); computing the system matrix values $S_{n,k}$; performing the original static image reconstruction, and computing elements of the the static segmentation mask $\mathbb{M}^s_{k,j}$ (10); and initializing elements of the dynamic mask $\mathbb{M}^d_{k,j}$ (11) and the integer segmentation mask $M_{k,j}$ (12).
2) *Initialization*: performing spline-based dynamic reconstruction in order to initialize the factor functions and coefficients.
3) *Refinement*: performing iterative refinement of the factors and factor coefficients.

The principal steps undertaken during these three stages are provided in Algorithm 1, while more detailed descriptions of stages 2 and 3 are provided in Algorithms 2 and 3, as defined below. SIFADS (Algorithm 1) takes as input the system matrix S, the dynamic sinogram P, and tissue segmentation information expressed as the static mask $\mathbb{M}^s$ created from the static reconstruction in the pre-processing stage using (10). The initial mask is generated in line 4 from $\mathbb{M}^s$ by (12), and the basis functions f^0 and their respective coefficient matrices are then initialized. The spline-based algorithm **SP** (see Algorithm 2) is run subsequently in line 9. Its output coefficients are then used to create initial factors in lines 11-12 by averaging tissue-wise voxels, and another run of **SP** is performed to determine the initial set of coefficients C^1 (lines 13-14) for the FADS algorithm (line 16). The output 4D image is computed in line 18, and the TACs are produced (line 19) by averaging the time varying voxel values within each segment once again using $\mathbb{M}^s$.

Algorithm 1. General steps of the SIFADS algorithm.

1: **// STAGE 1: DATA PREPARATION:**
2: $\mathbb{M}^s \leftarrow \{\text{Segmented Static Volume}\}$; *// Eq.(10)*
3: $\mathbb{M}^d \leftarrow \mathbb{M}^s$;
4: $\mathbb{M} \leftarrow$ **CreateMask**$(\mathbb{M}^s, \mathbb{M}^d)$; *// Eq.(12)*
5: **// STAGE 2: INITIALIZATION:**
6: **// Bsplines fitting**
7: $f^0 \leftarrow \{Bspline\ functions\}$;
8: $C^0 \leftarrow 1$;
9: $C^0 \leftarrow$ **SP**$(C^{[0]}, f^{[0]}, P, S, \mathbb{M}, \mathbb{M}^s)$; *// Algo.(2)*
10: **// Estimating initial curves and coefficients:**
11: $V(t) \leftarrow C^0 f^0$; *// Eq.*(5)
12: $f^1 \leftarrow Average(V(t), \mathbb{M})$;
13: $C^1 \leftarrow 1$;
14: $C^1 \leftarrow$ **SP**$(C^{[1]}, f^{[1]}, P, S, \mathbb{M}, \mathbb{M}^s)$;
15: **// STAGE 3: FADS REFINEMENT**
16: $(C^*, f^*, \mathbb{M}) \leftarrow$ **FADS**$(C^{[1]}, f^{[1]}, P, S, \mathbb{M}, \mathbb{M}^s)$; *//Alg(3)*
17: **// Estimate and output final TACs:**
18: $V(t) \leftarrow C^* f^*$;
19: $f \leftarrow Average(V(t), \mathbb{M})$;

Algorithm 2. MAP algorithm **SP** for estimating the coefficients C of given B-splines or time basis functions.

SP$(C, f, P, S, \mathbb{M}, \mathbb{M}^s)\{$
// Initialization
$\hat{P} \leftarrow 1$; **// A vector equal to sinogram size**
$C^{[1]} \leftarrow 1$;
$\gamma_0 \leftarrow 5.0$; $\lambda_1^{[1]} = \lambda_2^{[1]} \leftarrow 0.0001$;
for i = 1 to NoIter **do**
  // Create mask
  $\mathbb{M}^d \leftarrow$ **Threshold**$(C^{[i]})$; *// Eq.(11)*
  $\mathbb{M} \leftarrow$ **CreateMask**$(\mathbb{M}^s, \mathbb{M}^d)$; *// Eq.(12)*
  $U \leftarrow \lambda_1^{[i]}\Omega(C^{[i]}, \mathbb{M}) + \lambda_2^{[i]}\Theta(C^{[i]}, \mathbb{M})$;
  $U' \leftarrow \frac{\partial U}{\partial C^{[i]}}$;
  $C^{[i+1]} \leftarrow \frac{C^{[i]}}{\sum(S^T\hat{P}f^T)+U'} \sum \left(S^T \frac{P}{\sum SC^{[i]}f} f^T\right)$;
  // Update regularization parameters
  $E \leftarrow ||SC^{[i+1]}f^{[i+1]} - P||_2^2$; **// Data fit error**
  $\gamma \leftarrow \gamma_0(\frac{E}{0.05||P||_2^2})^{1/4}$;
  $\lambda_1^{[i+1]} \leftarrow \frac{1}{\gamma}\frac{E}{\Omega(C^{[i+1]},\mathbb{M})}$;
  $\lambda_2^{[i+1]} \leftarrow \frac{1}{\gamma}\frac{E}{\Theta(C^{[i+1]},\mathbb{M})}$;
end for
return $C, \mathbb{M}\}$

Algorithm 2 shows the details of the spline-based algorithm that uses MAP optimization. Within the iterations the masks for tissue types are generated by thresholding the current (i-th iteration) set of coefficients $C^{[i]}$ and then by intersecting those with the segmentation $\mathbb{M}^s$ of the static reconstruction provided as an input (lines 8-9). Lines 10-13 create the constraints and use that to update the coefficients as per the MAP optimization technique. Within the loop the tuning parameters are also updated in lines 15-17 as described in the next subsection.

Algorithm 3. MAP algorithm for the FADS method.

1: **FADS**$(C, f, P, S, \mathbb{M}, \mathbb{M}^s)\{$
2: **// Initialization**
3: $\hat{P} \leftarrow 1$; **// A vector equal to sinogram size**
4: $C^{[1]} \leftarrow 1$;
5: $\gamma_0 \leftarrow 5.0; \quad \lambda_1^{[1]} = \lambda_2^{[1]} = \lambda_3^{[1]} \leftarrow 0.0001$;
6: **for** i = 1 to NoIter **do**
7: **// Coefficient optimization:**
8: $\mathbb{M}^d \leftarrow$ **Threshold**$(C^{[i]})$; *// Eq.(11)*
9: $\mathbb{M} \leftarrow$ **CreateMask**$(\mathbb{M}^s, \mathbb{M}^d)$; *// Eq.(12)*
10: $U_1 \leftarrow \lambda_1 \Omega(C^{[i]}, \mathbb{M}) + \lambda_2 \Theta(C^{[i]}, \mathbb{M})$;
11: $U_1' \leftarrow \frac{\partial U_1}{\partial C^{[i]}}$;
12: $C^{[i+1]} \leftarrow \frac{C^{[i]}}{\sum (S^T \hat{P} f^{T[i]}) + U_1'} \sum (S^T \frac{P}{\sum SC^{[i]} f^{[i]}} f^{T[i]})$
13: **// Factor optimization:**
14: $U_2 \leftarrow \lambda_3 \Phi(f^{[i]})$;
15: $U_2' \leftarrow \frac{\partial U_2}{\partial f^{[i]}}$;
16: $f^{[i+1]} \leftarrow \frac{f^{[i]}}{\sum (SC^{[i+1]})^T \hat{P} + U_2'} \sum (SC^{[i+1]})^T \frac{P}{\sum SC^{[i+1]} f^{[i]}}$
17: **// Update regularization parameters**
18: $E \leftarrow ||SC^{[i+1]} f^{[i+1]} - P||_2^2$; **// Data fit error**
19: $\gamma \leftarrow \gamma_0 (\frac{E}{0.05||P||_2^2})^{1/4}$;
20: $\lambda_1^{[i+1]} \leftarrow \frac{1}{\gamma} \frac{E}{\Omega(C^{[i+1]}, \mathbb{M})}$;
21: $\lambda_2^{[i+1]} \leftarrow \frac{1}{\gamma} \frac{E}{\Theta(C^{[i+1]}, \mathbb{M})}$;
22: $\lambda_3^{[i+1]} \leftarrow \frac{1}{\gamma} \frac{E}{\Phi(f^{[i+1]})}$;
23: **end for**
24: **return** $C, f, \mathbb{M}\}$

Algorithm 3 describes the FADS algorithm. Here, lines 8-12 are similar to the steps used in the spline-based algorithm for determining the array C with a fixed factor array f. Subsequently the factors are determined in line 16, and the smoothness constraints are created in lines 14-15. The constraints' tuning parameters are updated in lines 18-22 as in the spline-based algorithm (2).

The functions **Threshold**() and **CreateMask**() in steps 8-9 in both Algorithm 2 and Algorithm 3 are computed using (11) and (12), respectively. The updating MAP-EM formulas in step 12 in Algorithm 2 and in step 16 in Algorithm 3 were derived to maximize the likelihood function (9) with respect to the C and f arrays [17][20].

D. Regularization Weighting Parameters

Choosing appropriate weights for multiple constraints is a difficult task. Instead of manually and exhaustively experimenting to find the best set of values, we used a method originally developed by Ito et al [19], [21] to dynamically update these values in each iteration. The basic principle of this method requires maintaining a balance between the data fitting and regularization terms. This is achieved by comparing the error levels using the least squares norm of the fit of the data and the values of the three regularization terms. Then, according to the comparison, the regularization weights are updated within iterations to keep the desired balance. The resulting expressions for updating the weight parameters are illustrated in Algorithm 2, steps 14-17 and Algorithm 3, steps 18-22. The initial value of γ_0 in step 5 in both Algorithms 2 and 3 was chosen according to the value used in [19]. The regularization parameters are monitored until the change from iteration to iteration is relatively small. The coefficients are also analyzed where convergence is determined when the error in the fit does not change by more than some convergence criteria. This technique provides an automatic method to choose the correct weighting parameters. In our experiments we found that the SIFADS algorithm provided nearly the same relative weights and the same solution as when we manually determined the optimum weighting parameters. We also found that the estimated coefficients obtained either from simulated or from real data were smooth and the tissues were well separated as desired.

III. Methods: Simulations and Experimentation

In this section we provide the numerical evidence of successful application of the SIFADS algorithm. The ability of our method to handle inconsistent projections was demonstrated using simulated dynamic SPECT studies. Then, the algorithm was applied to the dynamic SPECT studies of a canine subject and a murine subject.

A. Simulations

The initial validation of SIFADS was performed by applying the algorithm to simulated projection data and comparing the reconstruction results to the known input data. All simulations used the torso portion of the NCAT phantom [22], [23]. Three types of time-activity curves were generated for each simulation: the input function (tracer concentration in the blood pool) $f_B(t)$, the myocardium TAC $f_M(t)$, and the liver TAC $f_L(t)$. The input function $f_B(t)$ was drawn by hand, and the tissue curves were computed from it by using a single-compartment model with physiologically plausible uptake and washout parameters for each region. Simulated SPECT data were modeled to correspond to the geometry attainable by our GE Millennium VG3 SPECT camera. The projections were generated by forward-projecting the known simulated distributions. The forward projections were computed using the same system matrices used later in the real SPECT experiments described in Sections IV-B for a canine subject and IV-C for a rat subject. For the pinhole-collimator, a $80 \times 80 \times 80$ section of the NCAT phantom was used; $I = 90$ one-second views were generated over a 360° rotation, with 128×88 projection bins per view. For the parallel-projection case, a $64 \times 64 \times 41$ section of the phantom was used; seventy two one-second views of 64×64 bins were generated. Real objects are continuous so a limitation in the simulation was that projections were

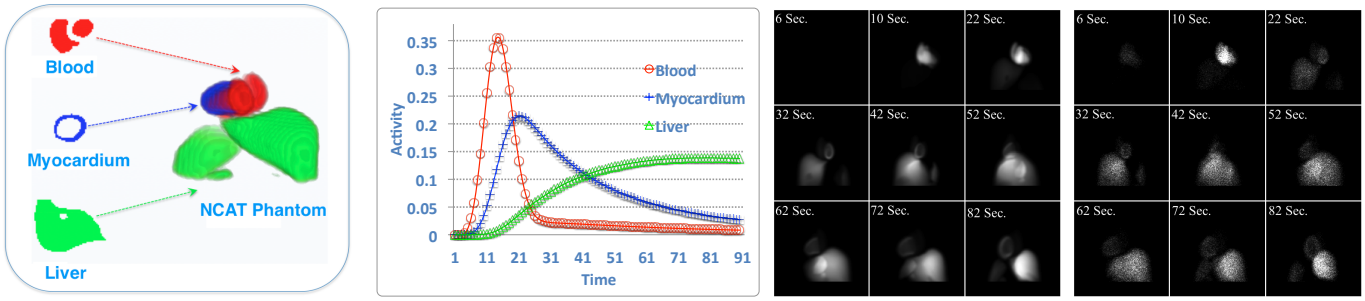

(b) (c) (d) (e)

Fig. 2. Set-up of a simulated dynamic SPECT study using the NCAT phantom. (a) Coefficient distributions generated for the blood, myocardium, and liver. (b) Selected TACs: blood input function, myocardium, and liver. (c) Samples of projections generated without noise added. (d) Samples of projections generated with Poisson noise added.

simulated using a discrete system matrix applied to a discrete source distribution. In order to simulate the dynamic data, the phantom volumes were segmented into three ROIs: blood pool inside myocardium cavity, myocardium, and liver. The i^{th} projection view were simulated by forward projecting the i^{th} realization of the phantom along the angle that corresponded to the $t = t_i$. The activity inside the phantom during the i^{th} time interval (t_{i-1}, t_i) was assumed to be constant. The generated values were used as the variance in generating Poisson pseudo-random numbers for the projection values. Another limitation was that the simulation did not replicate continuous rotation as was the case in the actual experiments. Twenty datasets with different input functions were used for each pinhole or parallel-hole collimator geometry model. The set-up of the simulation studies is illustrated in Fig. 2.

B. Canine Imaging Study

A GE Millennium VG3 Hawkeye SPECT/CT camera with low-energy high-resolution parallel-hole collimators was used to acquire data from a canine subject. The rest-study was performed with the detector heads in H-mode rotating continuously. Injection of 3.7 mCi (1.37×10^8 Bq) of ^{201}Tl was administered at the onset of the acquisition that continued for 20 minutes. Then a stress-study was performed by injecting 250 μg/kg/min of adenosine at an infusion rate of 1.5 ml/min. The dynamic scan started immediately upon injection of 15 mCi (5.55×10^8 Bq) of ^{99m}Tc-sestamibi approximately 3.5 min after the start of the adenosine stress. The scan continued acquiring 20 tomographic rotations. For each rotation, two sets of 72 one-second projections over 360° were acquired. Each view contained 64×64 projection bins. The bin dimensions were 4.42 mm. According to the vendor specifications, the detector resolution is 100 mm when using a low-energy high-resolution (LEHR) collimator and 3/8 inch crystal is 7.7 mm. The system matrix was generated to reconstruct the acquired static and dynamic projections. The gamma-ray attenuation was modeled using the attenuation map acquired using the X-ray CT of the SPECT/CT camera. The collimator blur was modeled using an empirically measured blurring kernel as described in the Appendix in [30].

C. Rat Pinhole SPECT Study

Projection data of a rat subject were acquired using the same dual-detector GE Millennium VG3 Hawkeye SPECT/CT system as described above equipped with pinhole collimators. Each collimator had a 2×1.5 mm (transaxial $\times$ axial dimensions) pinhole 25 cm above the center of the detector. The active area of each projection view contained 128×88 (lateral by axial) bins with an intrinsic spatial resolution of 4.6 mm and an energy resolution of 9.8%. The rat was anesthetized first and then injected with 1 mCi (3.70×10^7 Bq) of ^{201}Tl and scanned for 12 rotations. Then, the rat was injected with 5 mCi (1.85×10^8 Bq) of ^{123}I-MIBG and imaged for another 60 tomographic rotations. Each complete rotation consisted of 90 angular frames per detector head acquired every second (2 opposing heads were used). The system parameters and the acquisition protocol for this series of rat experiments are described in more detail in [7] and [8]. Analysis of the penetration and scatter through the pinhole for this system is given in [33]. The system matrix was constructed taking into account the collimator blur. The attenuation and scatter were not included. In the past, we tried attenuation modeling for rats, but no major improvements were noticed, primarily because the slice resolution of our Hawkeye CT did not provide sufficient resolution for small animals such as rats.

D. Evaluation of Results

The final output of SIFADS are three results: (1) final factors, (2) corresponding 3D coefficient for each factor, and (3) 4D reconstructed image (the dynamic series of 3D images) computed by multiplying these two. Furthermore, the tissue-specific TACs are also computed by averaging the TACs for the corresponding voxels in the tissue-segments, using the mask. In the simulation experiments, when the ground truth used for generating the dynamic datasets was known, we evaluated the spatial and temporal accuracies of the algorithm from the final reconstructions.

Spatial accuracy was measured from the estimated coefficients of each tissue type. The algorithm automatically segmented the imaged volume into a number of tissue types and estimated the coefficients for each segment. The segmentation was evaluated using the dice similarity coefficient (DSC) technique, as described in [26], [27]:

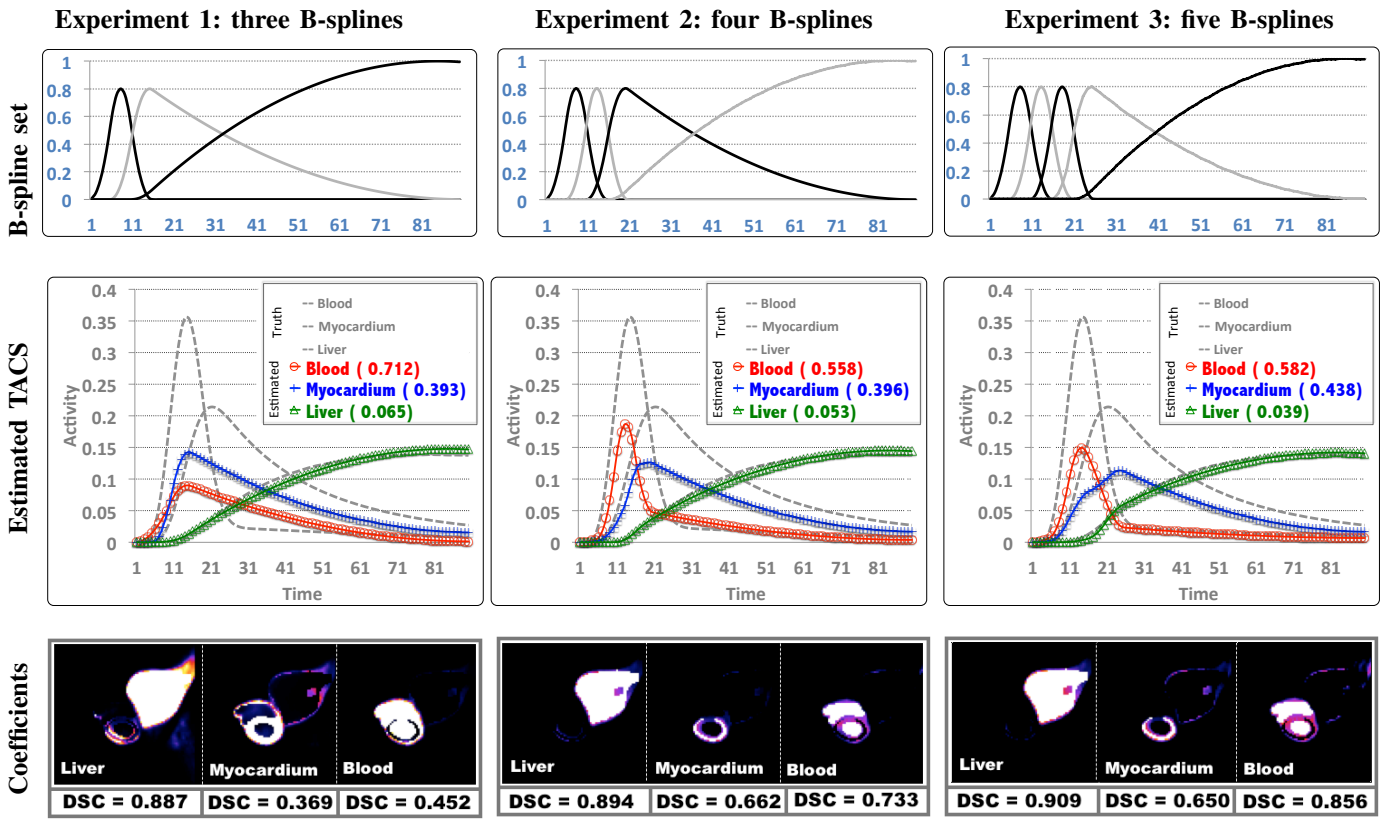

Fig. 3. Spline method in simulation: Illustration of the spline-based method applied to reconstruct a simulated dynamic dataset. Each column represents an experiment attempting to recover the original TACs using a different set of B-splines. *Top row*: Sets of basis functions used in the reconstruction: three, four, and five temporal B-splines. *Middle row*: Reconstructed TACs for the three numerical experiments. The RMS of each curve is included in parentheses in the corresponding legend. *Bottom row*: Estimated tissue distributions for the three experiments (These are coefficient values and the colors have no intrinsic meaning). The best estimation was achieved using four B-splines (second column).

$$DSC(\hat{C}_j) = \frac{2 \times |\hat{C}_j^{est.} \cap \hat{C}_j^{true}|}{|\hat{C}_j^{est.}| + |\hat{C}_j^{true}|}, \tag{17}$$

where $\hat{C}_j^{est}$ denoted the estimated coefficients of factor j or tissue type $j \in$\{Blood, Myocardium, Liver\}, $\hat{C}_j^{true}$ denoted the binary mask of the region of interest of tissue type j, and $|C|$ indicated the number of voxels in C. Both the estimated and ground truth were converted to a binary format using (11). DSC=1 means the segmentation is 100% accurate, and for DSC=0 the segmentation is completely inaccurate [28].

Temporal accuracy was measured by computing the Root Mean Square (RMS) between the reconstructed TACs and the known ground truth:

$$RMS(TAC_j) = \sqrt{\frac{\sum_i \left[(TAC_j^{est.})_i - (TAC_j^{true})_i\right]^2}{\sum_i (TAC_j^{true})_i^2}}, \tag{18}$$

where $(TAC_j^{est.})_i$ denotes the value of the estimated time activity curve of tissue type j at time t_i and $(TAC_j^{true})_i$ is the corresponding ground truth TAC value used as an input in the simulation. When the RMS goes to zero, this corresponds to a perfect recovery of the TAC.

IV. Results

In this section we present the results of the proposed algorithm and compare it to the results of the spline-based and FADS methods. The three algorithms were implemented and tested on an Apple Xserve (Early 2009) running Mac OS X server. The machine had two dual quad-core 2.93 GHz Xeon processors and 12 GB of RAM. After implementation in C, the three algorithms were tested against the simulated data described in the previous section with the same number of iterations. Specifically, the total number of iterations for the spline-based and FADS algorithms was set to 30. The number 30 was chosen for all three algorithms where it was determined that the objective function for each algorithm had converged based upon a convergence criterion. One algorithm might have converged in fewer iterations but the number was chosen such that all three had converged. For SIFADS, the number of iterations was set to 10 in each stage, which adds up to a total of 30. For a volume of size 64×64×41 voxels and a dynamic sinogram of 64×41 pixels by 72 projections, the total CPU running time to perform a complete dynamic reconstruction was 9.4 minutes for the spline-based algorithm, 15.1 minutes for the FADS algorithm, and 16.9 minutes for the SIFADS algorithm.

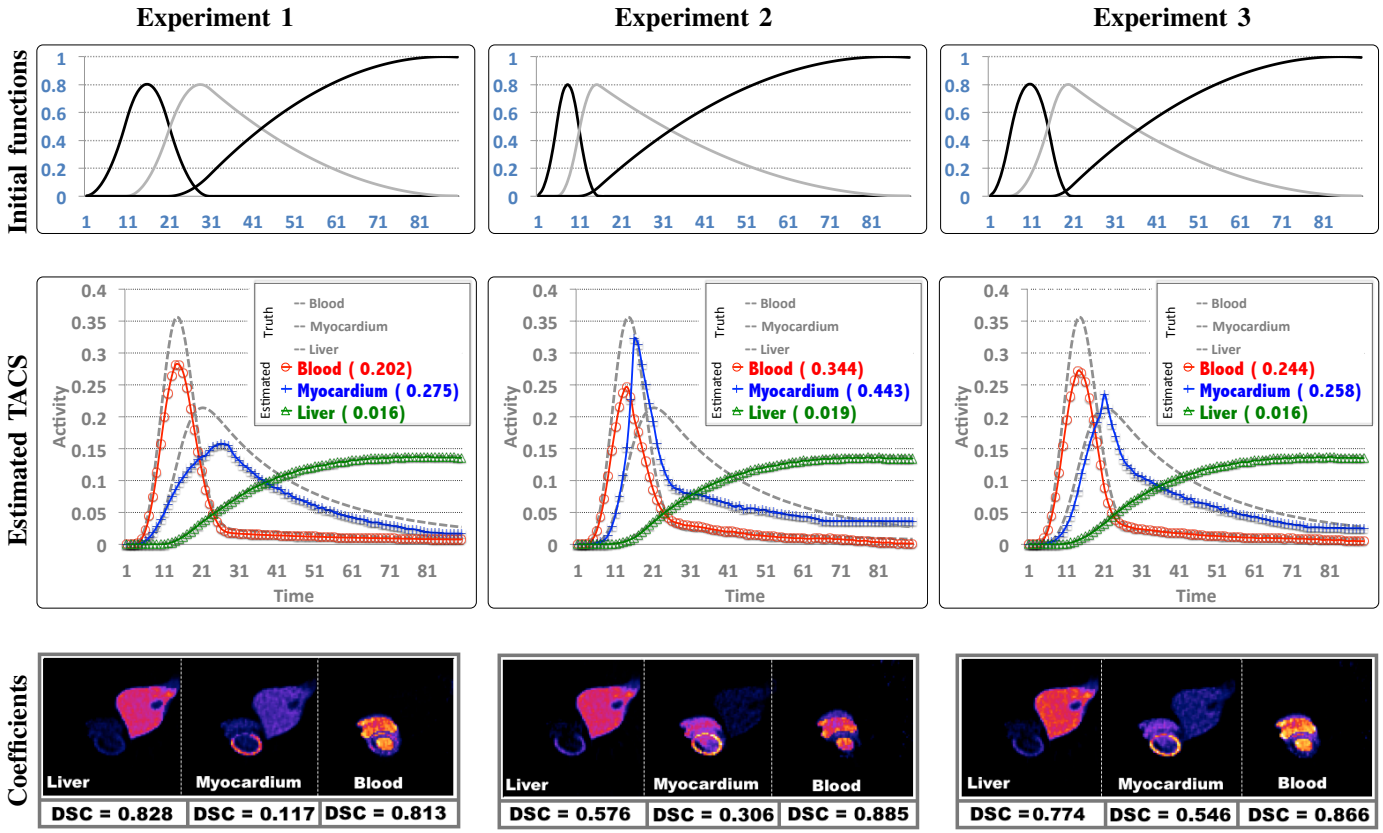

Fig. 4. FADS in simulation: Illustration of the FADS method applied to reconstruct a single dynamic dataset. Each column represents an experiment attempting to recover the original TACs using a different initial set of initial temporal basis functions. *Top row*: Three initial guesses of the three factors. *Middle row*: TACs reconstructed for the corresponding initial guesses. The RMS of each curve is included in parentheses in the corresponding legend. *Bottom row*: Reconstructed tissue coefficient distributions (These are coefficient values and the colors have no intrinsic meaning). Slight differences in the initial choice of the basis functions result in significantly different estimation of TACs and tissue concentration.

A. Simulated SPECT Studies

Over twenty simulated projection datasets with different input functions and uptake and washout parameters were generated. Each dataset was reconstructed with three different approaches: Splines-based, FADS, and SIFADS. For all numerical experiments, the accuracy of the TAC estimation was evaluated using the RMS (18) and the quality of the tissue separation was evaluated by the DSC (17).

The performance of the spline-based method is illustrated in Fig. 3 for one of the input datasets. The top row shows three different choices of the temporal basis set with three, four, and five B-splines. The coefficients for each of these sets of B-splines were estimated using Algorithm 2 presented in the Section II-C. The myocardium, blood and liver TACs were extracted by averaging across each ROI (middle-row). Fig. 3 clearly illustrates that the performance of the spline-based method critically depends on the selection of the basis, producing results with poorly recovered TACs (large RMS values shown in the middle row) and segmentations (DSC values smaller than one as shown in the bottom row). Having some prior estimate of the TACs could facilitate a better choice of the B-spline basis. In PET, this could be achieved using the *head curves* as suggested in [29]; however, this approach is not available in SPECT due to the limited number of projections at each time frame.

The performance of the FADS method is illustrated in Fig. 4 using a single dynamic dataset and three choices of initial guesses for the tissue TACs (top-row). The number of factors was selected to be equal to the number of segments obtained from the static image, which was reconstructed from later aggregated projections. For example, the number of factors selected in the rat study presented in the Fig. 8 was three, the same as the number of segments observed in the static image. Our experiments show that using a higher or smaller number of factors provide less accurate results. The example results in Fig. 4 demonstrate extreme sensitivity of the method to the initial choice of the factor functions. The RMS of the estimated TACs and the DSC of the segmentation accuracy are shown in the middle and bottom rows of the figure.

Fig. 5 shows three examples of the SIFADS method applied to three simulated dynamic projection datasets. The quality of both the reconstructed TACs and the estimated tissue distribution is superior to that achieved using only the spline-based or FADS methods. Note that the input curves in the first column in Fig. 5 are the same as those used in Figs. 3 and 4, while the curves in the middle and the right columns in Fig. 5 are more complex.

In Fig. 6, we compare the two numerical measures of the

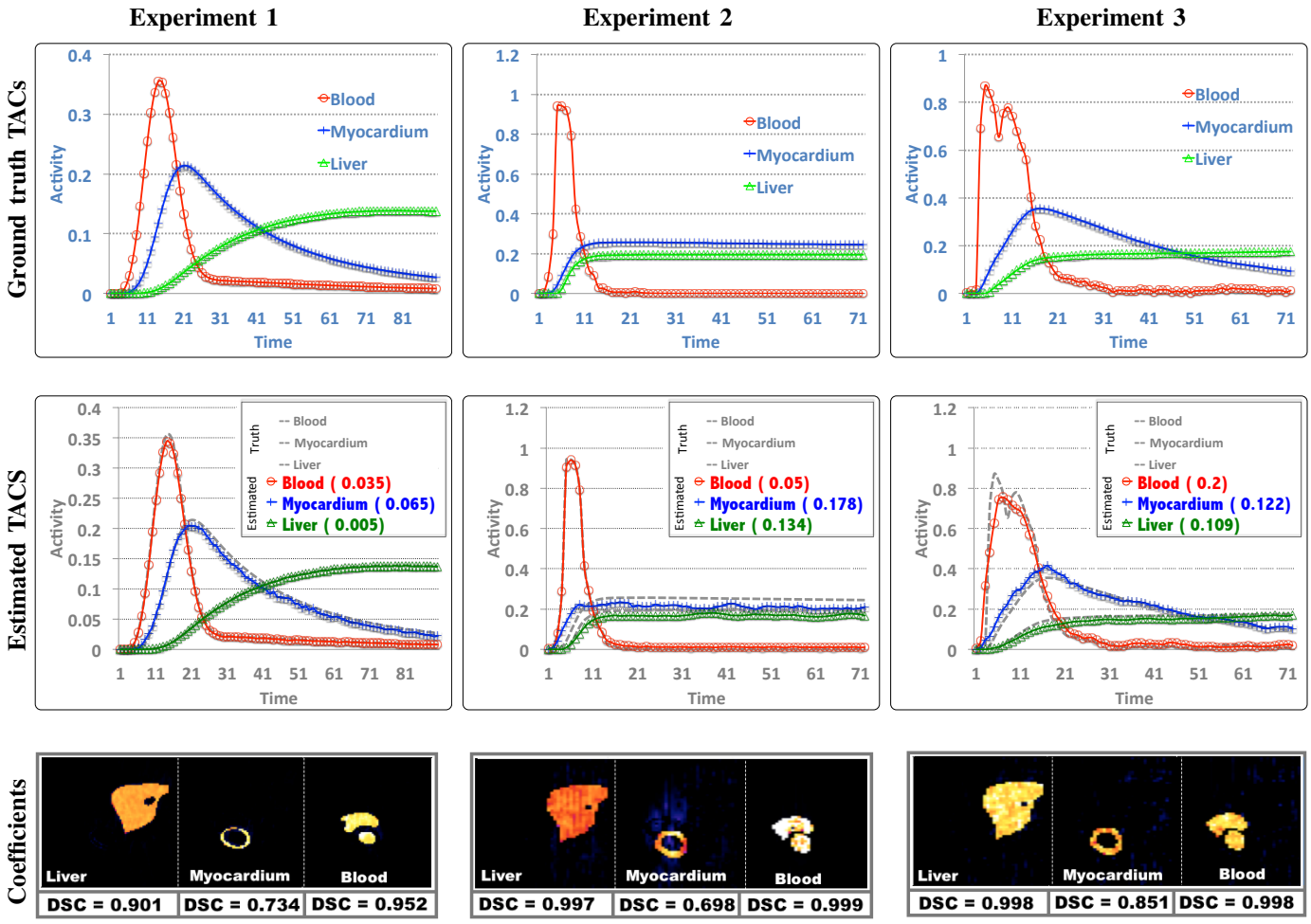

Fig. 5. SIFADS in simulation: Results of SIFADS algorithm for three simulated projection datasets. *Top row*: Simulated TACs. *Middle row*: Reconstructed TACs plotted against the ground truth curves (dotted gray lines). The RMS of each curve is included in parentheses in the corresponding legend. *Bottom row*: Reconstructed tissue distributions (These are coefficient values and the colors have no intrinsic meaning).

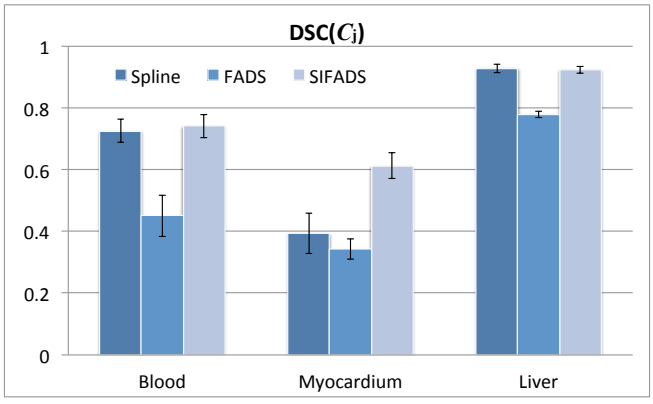

(a) Estimated coefficients and their DSC

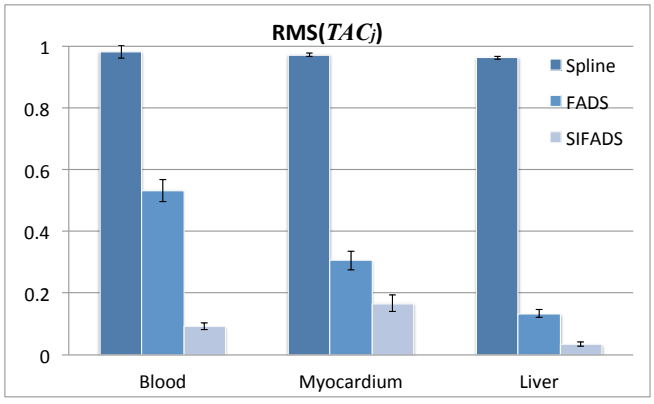

(b) Estimated coefficients and their DSC

Fig. 6. Different algorithm performance results from ten numerical experiments with different input TACs. (a) Mean dice similarity coefficient measure for the myocardium, blood, and liver regions computed using (17). (b) Mean Root Mean Square error of the estimated TACs computed using (18).

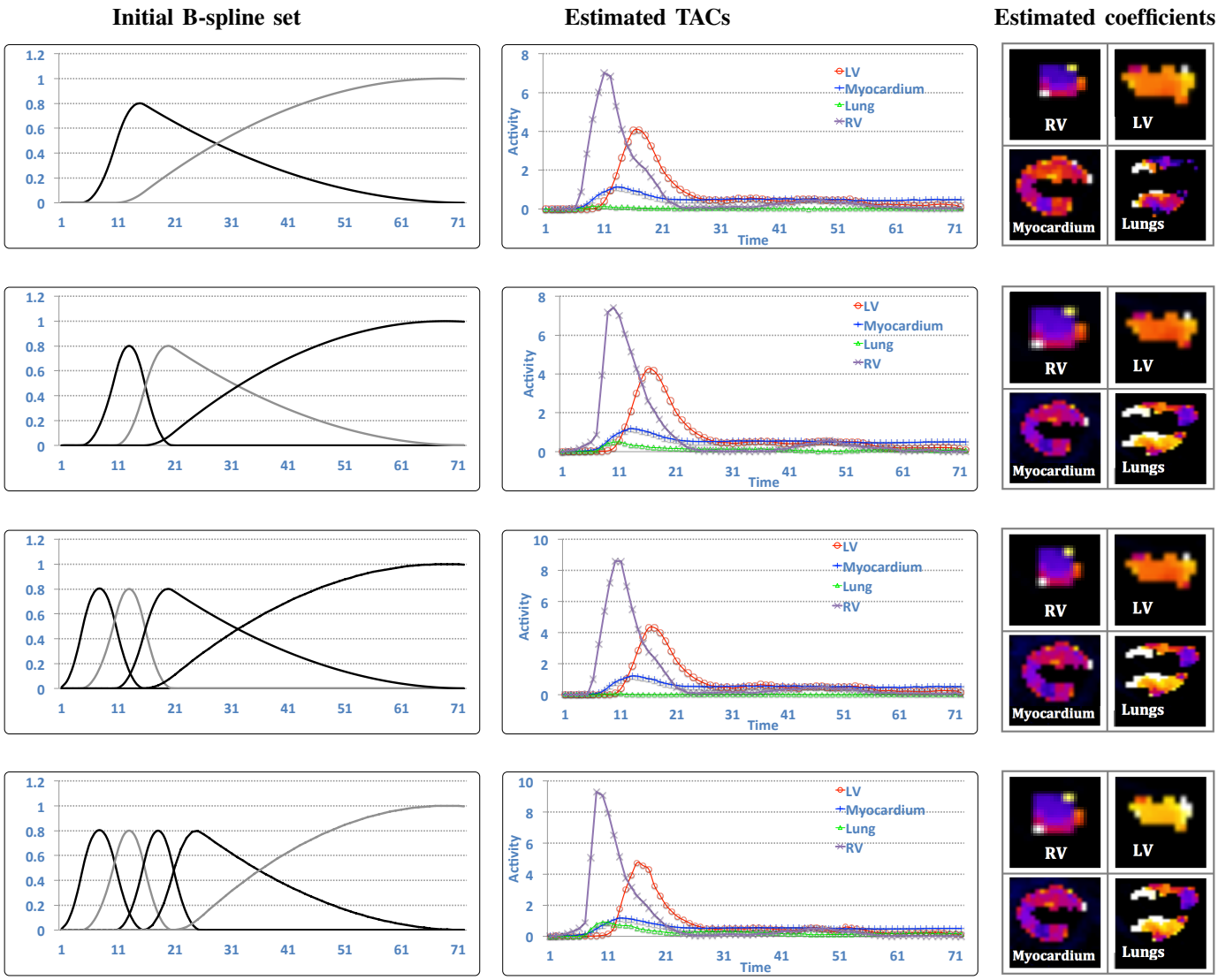

Fig. 7. Caine SPECT: Results of the SIFADS method applied to the canine dataset as described in Section IV-B. Four different sets of the initial factor functions (left column) produce very similar TACs (middle column) and tissue distributions (right column). The similarity of the resulting TACs is also confirmed by small values of pair-wise RMS differences provided in Table I.

reconstruction quality for the three algorithms based on the application of these algorithms to ten simulated datasets with different hand-drawn input TACs. The performance of the SIFADS algorithm is comparable or superior to the performance of the spline-based or FADS methods.

B. Canine SPECT Study

Four different choices of the B-spline set were used to form the initial guess for the FADS portion of the algorithm. The results of all four SIFADS reconstructions of the canine dynamic SPECT data are shown in Fig. 7. The figure shows that reconstructing four independent TACs allowed us to recover the tracer concentration in the right ventricle.

Experiments	RV	LV	Myocardium	Lung
1-2	0.1752	0.0198	0.0143	0.0197
1-3	0.1874	0.0197	0.0121	0.0223
1-4	0.1543	0.0228	0.0247	0.0310
2-3	0.0261	0.0075	0.0076	0.0129
2-4	0.0475	0.0122	0.0161	0.0179
3-4	0.0549	0.0107	0.0190	0.0264

TABLE I
PAIRWISE RMS DIFFERENCES, CANINE DATA RECONSTRUCTIONS, FIG. 7.

In order to measure the level of similarity of the TACs computed using different initial estimates of the factors, we computed the pairwise differences between RMSs of the four reconstruction results. The differences were computed using the same approach as in (18), with TAC_j^{est} and TAC_j^{true} substituted by two versions of the reconstruction. The RMS differences between each pair of the four experiments provided in Table I show that the algorithm converged to the same

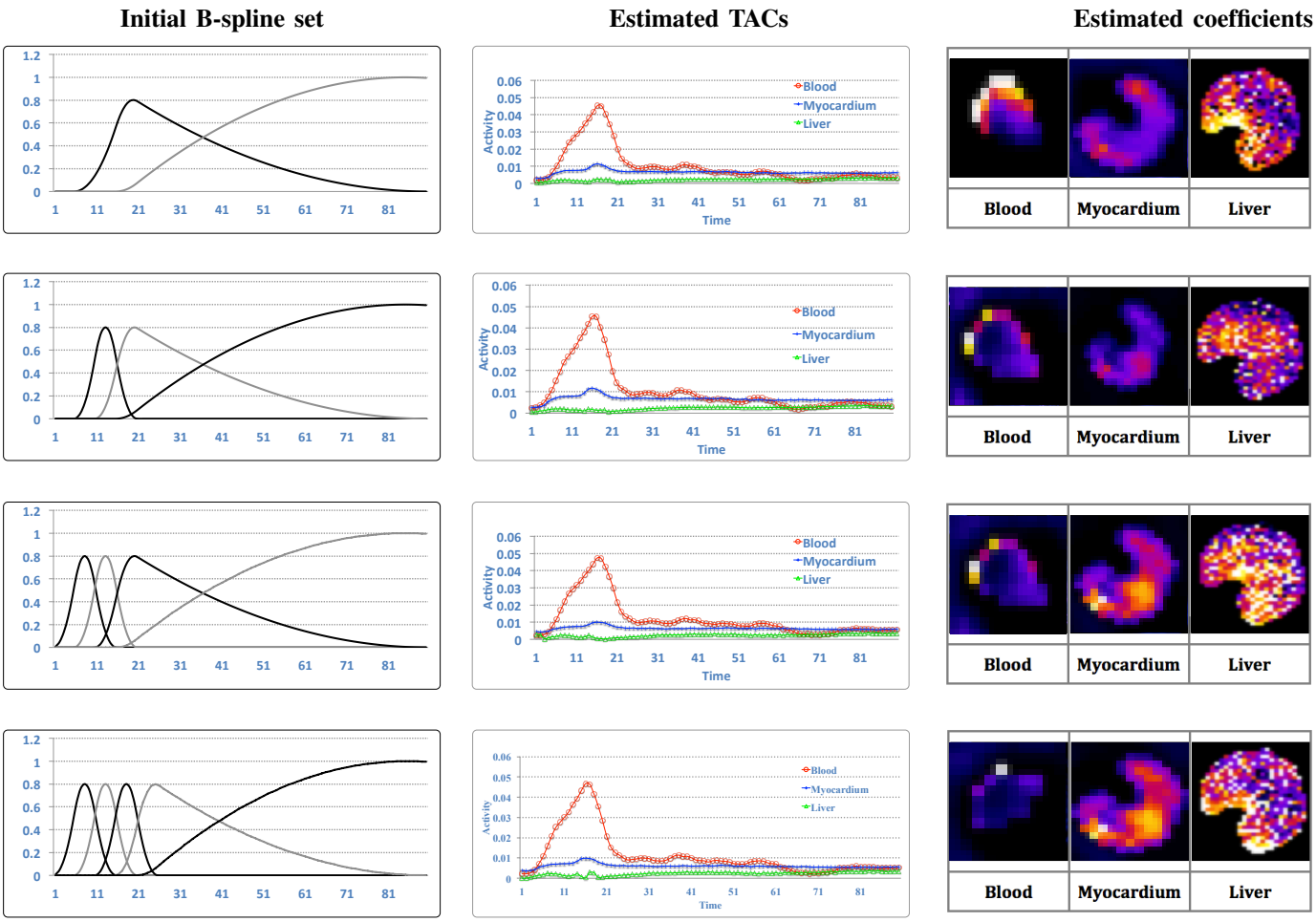

Fig. 8. Murine SPECT: Results of four reconstructions with different initializations for estimating time activity curves from the dynamic pinhole SPECT projections in the rat imaging experiment. Column one shows the B-splines used as initial estimates of the factors in each case. Column two shows the estimated TACs. Column three shows the estimated coefficients. Table II below shows the RMS differences between each pair of the four reconstructions. The difference values are small, confirming that the estimated TACs' low dependence on the initial guess of the factor functions.

activity curves for all four initial choices of f, illustrating stability of the SIFADS algorithm.

C. Rat SPECT Study

The dynamic reconstruction using SIFADS was performed to estimate TACs of three ROIs including blood pool in the left ventricle, myocardium, and liver. Fig. 8 shows the estimated TACs for the dynamic cardiac SPECT of a rat with several different choices of B-splines for forming the initial array of the temporal basis f. The pair-wise RMS differences (for the four reconstructed experiments) computed using (18) are shown in Table II. In all instances, the TACs converged to the same curves, confirming the stability of our algorithm.

Experiments	Blood	Myocardium	Liver
1-2	0.00020	0.00016	0.00027
1-3	0.00175	0.00046	0.00059
1-4	0.00115	0.00061	0.00046
2-3	0.00170	0.00057	0.00044
2-4	0.00111	0.00075	0.00037
3-4	0.00070	0.00036	0.00053

TABLE II
PAIRWISE RMS DIFFERENCES, RAT DATA RECONSTRUCTIONS, FIG. 8.

V. Discussion

The new algorithm of reconstructing time-dependent images from dynamic projection data presented in this manuscript has three major contributions. First, our method combines the spline-based and FADS methods to provide accurate recovery of time activity curves. Second, our SIFADS method utilizes the iterative optimization procedure with adaptive adjustment of weighting factors of spatiotemporal constraints, which efficiently segments different tissue types. Finally, we validated our method using both simulated projection data and two real SPECT datasets from animal studies.

The main challenge of dynamic SPECT reconstruction is the underdetermined nature of the tomographic problem and the large number of unknowns. The large size of the array of unknown coefficients or intensities to be reconstructed makes the computation slow. The fact that the number of unknowns

is far greater than the number of equations in the discrete formulation of the tomographic problem imposes the necessity for various constraints. Sometimes, some of the constraints may alter the solution, making it less accurate. The simplest example is the use of smoothing regularization terms, which may blur tissue boundaries. Alternatively, the tissue separation regularization term that we use may enforce artifacts by preventing partial volume correction in the boundary voxels. This results in spillover cross-contamination of the factor functions for different tissues [24]. We fully realize the caveats of the constraints; however, in the dynamic SPECT case the inaccuracies introduced by the regularization constraints represent the necessary price that we have to pay for the very ability to obtain a stable estimate of the post-injection dynamic tracer concentration.

One other area where the stability of the algorithm and the ability to find a unique solution to the inverse problem takes priority over other considerations is the application of various corrections in our reconstruction. In particular, we believe that correcting for organ motion is not plausible for the considered dynamic SPECT problem. Current motion correction approaches involve subdividing the projection data into subsets that correspond to different spatial configurations. This subdivision would make the problem even more ill-posed, making a stable solution impossible, because there would not be sufficient projection data points to enable adequate motion-corrected reconstruction. However, one would expect to obtain stable solutions by incorporating a projection sinogram-level correction [31], [32]. This is an approximate method that can produce only partial corrections, but it is appealing because it does not reduce the amount of projection data used to solve the dynamic problem.

Finally, there is some similarity between our approach and the robust principal component analysis with low rank and spares matrix optimization [34] that has applications in MRI [35] and in PET [36]. These cited authors decompose data into two additive components for the purpose of sparsification: a static low rank matrix and a sparse motion noise matrix. In contrast, we decompose data into two multiplicative components: a few factor functions and the corresponding coefficient matrices.

The primary purpose of developing SIFADS was to address the sensitivity of FADS to the initial choice of factors. Even still, SIFADS remains dependent on a prior knowledge of the number of significant factors (tissue types having distinct time activities) and an accurate selection of ROIs corresponding to the factors that best represent the kinetics of the tracer. For a particular dynamic imaging protocol, we found that it took some effort to satisfy these two conditions. The SIFADS method will fail if the wrong number of factors were selected or if the ROIs were poorly selected which can happen with noisy data. For each data set we determined (by trial and error) the correct number of factors and the mask for anatomical regions of interest that corresponded to particular factors such as right and left ventricular blood pools, and myocardial tissue. If the data are such that the acquisition does not capture the true kinetics of the tracer, then the SIFADS method cannot estimate true activity cures. Also it would be expected that if the data have several factors then the estimation becomes more challenging with increased errors in the estimated parameters and the increased potential of non-unique solutions. The accuracy of the SIFADS method improves as the timing resolution of the acquisition is improved, count statistics are improved, and the number of factors is small. A limitation of our present work is not having quantified the sensitivity of SIFADS to the accuracy of ROI selection.

VI. Conclusions

SIFADS, a hybrid algorithm combining spline-based and factor analysis methods, has been developed to estimate blood input function and myocardial tissue time activity curves. Our algorithm uses a combination of regularization functions that improve the estimation of the blood input function and tissue time-activity curves from the inconsistent projections acquired during the early rotations in dynamic SPECT imaging. The regularization functions exploit the anatomical structures obtained from the static reconstruction of the later reconstructed consistent frames. The relative weighting of the regularization terms changes adaptively during the iterative reconstruction process, allowing the optimal utilization of the tomographic projection data and the prior knowledge. Our method was validated using simulated SPECT projection data, and then applied it to two different types of real cardiac SPECT data acquired using slow gantry rotation. In simulation the method provided better segmentation as measured by the DSC: spline (0.369 - 0.909), FADS (0.117 - 0.885), and SIFADS (0.698-0.999); and better TACs as measured by RMS: spline (0.712 - 0.039), FADS (0.443 - 0.016), and SIFADS (0.2 - 0.005). The SIFADS algorithm provides a method for extracting kinetic information from a very difficult dynamic reconstruction problem involving the acquisition of data in rodent studies with slowly rotating gamma cameras mounted with pinhole collimators.

Acknowledgements

This work was supported in part by the National Institute of Biomedical Imaging and Bioengineering under grant R01EB00121 and the Heart, Lung, and Blood Institute of the National Institutes of Health under grant R01HL50663 and by the Director, Office of Science, Office of Biological and Environmental Research, Medical Sciences Division of the US Department of Energy under contract DE-AC02-05CH11231. Many thanks to the reviewers and to Jennifer Huber, Ph. D. for help in editing the manuscript.

References

[1] G. T. Gullberg, B. W. Reutter, A. Sitek, J. S. Maltz, and T. F. Budinger, "Dynamic Single Photon Emission Computed Tomography Basic Principles and Cardiac Applications," *Phys. Med. Biol.*, vol. 55, no. 20, pp. R111-R191, 2010.

[2] H. S. Khare, E. V. Dibella, D. J. Kadrmas, P. E. Christian, G. T. Gullberg, "Comparison of Static and Dynamic Cardiac Perfusion Thallium-201 SPECT," *IEEE Trans. Nucl. Sci.*, vol. 48, no. 3, pp. 774, 2001.

[3] T. H. Farncombe, A. M. Celler, D. Noll, J. Maeght, and R. Harrop, "Dynamic SPECT Imaging Using a Single Camera Rotation (dSPECT)," *IEEE Trans. Nucl. Sci.*, vol. 46, no. 4, pp. 1055-1061, 1999.

[4] M. A. Limber, M. N. Limber, A. Celler, J. S. Barney, and J. M. Borwein, "Direct Reconstruction of Functional Parameters for Dynamic SPECT," *IEEE Trans. Nucl. Sci.*, vol. 42, no. 4. pp. 1249-1256, 1995.

[5] B. W. Reutter, G. T. Gullberg, and R. H. Huesman, "Direct Least-Squares Estimation of Spatiotemporal Distributions From Dynamic SPECT Projections Using a Spatial Segmentation and Temporal B-Splines," *IEEE Trans. Med. Imag.*,vol. 19, no. 5, pp. 434-450, 2000.

[6] B. W. Reutter, G. T. Gullbergz and R. H. Huesman, "Effects of Temporal Modeling on the Statistical Uncertainty of Spatiotemporal Distributions Estimated Directly from Dynamic Cone-beam SPECT Projections," *IEEE Trans. Med. Imag.*, vol. 47, no. 15, pp. 2673-2683, 2002.

[7] B. W. Reutter, R. H. Huesman, R. Boutchko, K. M. Brennan, S. M. Hanrahan, and G. T. Gullberg, "Longitudinal Evaluation of Fatty Acid Metabolism in Normal and Spontaneously Hypertensive Rat Hearts With Dynamic MicroSPECT Imaging," *International Journal on Molecular Imaging*, vol. 54, no. 11, pp. 1938-1945, 2002.

[8] Y. Zan, R. Boutchko, Q. Huang, B. Li, K. Chen, G. T. Gullberg, "Fast Direct Estimation of the Blood Input Function and Myocardial Time Activity Curve from Dynamic SPECT Projections via Reduction in Spatial and Temporal Dimensions," *Medical Physics*, vol. 40, no. 9, pp. 092503, 2013.

[9] R. Dipaola, J. P. Bazin, et al., "Handling of Dynamic Sequences in Nuclear Medicine," *IEEE Trans. Nucl. Sci.*, vol. 29, no. 4, pp. 1310-1321, 1982.

[10] A. Sitek, E. V. R. Di Bella and G. T. Gullberg, "Factor Analysis with a Priori Knowledge Application in Dynamic Cardiac SPECT," *Phys. Med. Biol.*, vol. 45, no 9, pp. 2619-2638, 2000.

[11] A. Sitek, G. T. Gullberg,R. H. Huesman, "Correction for Ambiguous Solutions in Factor Analysis Using a Penalized Least Squares Objective," *IEEE Trans. Med. Imag.*, vol. 21, no. 3, pp. 216-225, 2002.

[12] Yi Su, Michael J. Welch, and K. I. Shoghi, "The Application of Maximum Likelihood Factor Analysis (MLFA) with Uniqueness Constraints on Dynamic Cardiac MicroPET Data," *Phys. Med. Biol.*, vol. 52, no. 8, pp. 2313-2334, 2007.

[13] J. Hu, R. Boutchko, A. Sitek, B. W. Reutter, R. H. Huesman, and G. T. Gullberg, "Dynamic Molecular Imaging of Cardiac Innervation Using a Dual Head Pinhole SPECT System," *Technical report*,LBNL-60008 , 2008.

[14] T. Humphries, et al, "Segmentation-based Regularization of Dynamic SPECT Reconstructions," *IEEE Nuclear Science Symposium Conference*, pp. 2849-2852, 2009.

[15] T. Humphries, et al, "Slow-Rotation Dynamic SPECT with a Temporal Second Derivative Constraint," *Med. Phys.*, vol. 38, no. 8, pp. 4489, 2011.

[16] T. Humphries, et al, "Effects of Attenuation in Single Slow Rotation Dynamic SPECT," *Phys. Med. Biol.*, vol. 57, no. 14, pp. N253-N256, 2012.

[17] E. Levitan, and G. T. Herman, "A Maximum a Posteriori Probability Expectation Maximization Algorithm for Image Reconstruction in Emission Tomography," *Medical Imaging, IEEE Transactions on* , vol. 6, no. 3, pp. 185,192,1987.

[18] G. T. Herman, and D. Odhner, "Performance evaluation of an iterative image reconstruction algorithm for positron emission tomography," *Medical Imaging, IEEE Transactions on*, vol.10, no. 3, pp. 336,346, 1991.

[19] K. Ito, B. Jin, and T. Takeuchi, "A Regularization Parameter for Nonsmooth Tikhonov Regularization," *SIAM Journal on Scientific Computing*, vol. 33, no. 3, pp. 1415-1438, 2011.

[20] P. P. Bruyant, "Analytic and Iterative Reconstruction Algorithms in SPECT," *J. Nucl. Med.*, vol. 43, no. 10, pp.1343-1358, 2002.

[21] K. Ito, B. Jin, and T. Takeuchi, "Multi-Parameter Tikhonov Regularization," *arXiv*:1102.1173, 2011.

[22] W. Paul Segars, D. S. Lalush, and B. M. W. Tsui, "A Realistic Spline-Based Dynamic Heart Phantom," *IEEE Trans. Nucl. Sci.*, vol. 46, no. 3, pp. 503-506, 1999.

[23] W. Paul Segars and B. M. W. Tsui, "Study of the Efficacy of Respiratory Gating in Myocardial SPECT Using the New 4D NCAT Phantom," *IEEE Trans. Nucl. Sci.*, vol. 49, no. 3, pp. 675-679, 2002.

[24] B. W. Reutter, R. Boutchko, R. H. Huesman, A. C. Sauve, and G. T. Gullberg, "Tissue Spillover Correction for Dynamic Pinhole SPECT Studies of Fatty Acid Metabolism in the Rat Heart," *IEEE Nuclear Science Symposium Conference*,10.1109/NSSMIC.5401782, 2009.

[25] R. Choksi, Y. van Gennip, and A. Oberman, "Anisotropic Total Variation Regularized L1-Approximation and Denoising/Deblurring of 2D Bar Codes," *arXiv*:1007.1035v2, 2011.

[26] T. Srensen, "A method of Establishing Groups of Equal Amplitude in Plant Sociology Based on Similarity of Species and its Application to Analyses of the Vegetation on Danish Commons," *Kongelige Danske Videnskabernes Selskab*, vol. 5, no. 4, pp. 1-34, 1957.

[27] L. R. Dice, "Measures of the Amount of Ecologic Association Between Species," *Ecology*, vol. 26, no. 3, pp. 297-302, 1945.

[28] K. H. Zou, et al, "Statistical Validation of Image Segmentation Quality Based on a Spatial Overlap Index," *Academic Radiology*, vol. 11, no. 2, pp. 178-189, 2004.

[29] E. T. Nichols, J. Qi, E. Asma, and M. R. Leahy, "Spatiotemporal reconstruction of list-mode PET data," *IEEE Trans. Med. Imag.*, vol. 21, no. 4, pp. 396-404, 2002.

[30] R. Boutchko, A. Sitek, and G. T. Gullberg, "Practical implementation of tetrahedral mesh reconstruction in emission tomography," *Phys. Med. Biol.*, vol. 58, no. 9, pp. 3001-3022, 2013.

[31] D. Eiland, Debasis Mitra, M. Abdalah, R. Butchko, and G. T. Gullberg, "Inter-frame and Intra-frame Motion Correction Tool," *IEEE Nuclear Science Symposium Conference*, pp. 2963-2966, 2012.

[32] D. Mitra, D. Eiland, T. Walsh, R. Bouthcko, and G. T. Gullberg, "SinoCor: a Clinical Tool for Sinogram-level Patient Motion Correction in SPECT," *Proc. SPIE, Medical Imaging*, Vol. 7962, article id: 79624V, pp. 5, 2011.

[33] Z. El Bitar, R. H. Huesman, R. Boutchko, V. Bekaert, D. Brasse, and G. T. Gullberg, "A detector response function design in pinhole SPECT including geometrical calibration," *Phys. Med. Biol.*, vol. 58, no. 7, pp. 2395-2411, 2013.

[34] E. J. Candès, X. Li, Y. Ma, and J. Wright, "Robust Principal Component Analysis?," *J. ACM*, Vol. 58, no. 3, pp. 11:1–11:37, 2011.

[35] B. Zhao, J. P. Haldar, C. Brinegar, and Z. Liang, "Low Rank Matrix Recovery for Real-time Cardiac MRI," *ISBI'10 Proceedings of the 2010 IEEE international conference on Biomedical imaging*, pp. 996–999, 2010.

[36] C. Jingyu, Y. Jaewon, E. Graves, and C. S. Levin, "GPU-enabled PET motion compensation using sparse and low-rank decomposition," *Nuclear Science Symposium and Medical Imaging Conference (NSS/MIC), 2012 IEEE*, pp. 3367-3370, 2012.